

Radicals Persistent above 300 °C: from Framework Design to Solar Vapor Generation

Xinhe Ye

Guangdong University of Technology

Lai-Hon Chung

Guangdong University of Technology

Kedi Li

City University of Hong Kong

Saili Zheng

Guangdong University of Technology

Wong Yan Lung

City University of Hong Kong

Zihao Feng

Guangdong University of Technology

Yonghe He

Guangdong University of Technology

Dandan Chu

City University of Hong Kong

Zhengtao Xu (✉ zhengtao@cityu.edu.hk)

City University of Hong Kong <https://orcid.org/0000-0002-7408-4951>

Jun He

Guangdong University of Technology

Article

Keywords:

Posted Date: April 7th, 2022

DOI: <https://doi.org/10.21203/rs.3.rs-1460612/v1>

License: © ⓘ This work is licensed under a Creative Commons Attribution 4.0 International License.

[Read Full License](#)

Version of Record: A version of this preprint was published at Nature Communications on October 17th, 2022. See the published version at <https://doi.org/10.1038/s41467-022-33948-9>.

Abstract

The strong, stable radical signal is forged from two levels of structural design. On the molecular level, we fused terephthalic acid with two 1,4-dithiin (-S-CH = CH-S-) units to afford a polycyclic (3-ring), sulfur-rich linker (TTA) with versatile reactivity—*e.g.*, for generating stable radicals. On the solid-state level, the linker was crystallized with Eu(III) to form EuTTA as a 3D metal-organic framework (MOF) featuring stacks of TTA molecules along the Eu-carboxyl rod domain. As revealed by single-crystal X-ray diffraction, the slightly loosened packing of the TTA molecules allows wiggle room for uniquely selective thermal reactions: among the repeat of three TTA molecules along the stack, one first transforms into benzodithiophene (by extruding one S atom from each of the dithiin wings) at 230°C, while the other two TTA molecules only react at higher temperatures (*e.g.*, 300–350°C)—to form bis(dithiole) and other sulfur-stabilized radicals, as well as covalent crosslinks thereof. Aside from the highest thermal stability observed of its radicals (above 300°C), the black MOF product (*i.e.*, EuTTA-350; obtained from heating at 350°C) remain crystalline, and water/air-stable, and features strong broad absorption in the visible and near IR region. As a result, EuTTA-350 achieves highest efficiencies in both photothermal conversion and solar-driven water evaporation among MOF materials, holding promise in solar steam generation.

Introduction

Organic radicals are often reactive and unstable species, because their unpaired electrons tend to seek each other out for covalent bonding, and for achieving the stable doubly occupied (closed shell) configuration. Stabilized radicals,^{1,2} on the other hand, allow for many uses in polymer functionalization,³⁻⁵ solar cells,^{6,7} magnetic materials design,⁸⁻¹¹ and bioimaging/cancer therapy.^{12,13} To enhance stability, bulky groups can be piled around the radical center to afford steric protection;^{2,14,15} and large conjugate molecules can be used to host the radical center, so as to delocalize the unpaired electron and to mitigate its open-shell character.¹⁶⁻²¹ Both are known molecular design strategies that can yield stunning results, like the dicarbonyl radical cation persistent even at 200 °C,¹⁴ and 200 °C is indeed the upper limit achieved so far for radicals. In this light, the organic radical species here, persistent above 300 °C, is a record breaker—by a long shot.

Underlying this discovery is a crosscutting approach that synergizes molecular design and spatial control in the solid state. Molecule TTA (1, 4, 5, 8-tetrathiaanthracene-9, 10-dicarboxylic acid, Scheme 1) is equipped with the carboxylic groups widely used for building metal-organic frameworks (MOFs);²²⁻²⁵ and the key design lies in the two wings of 1,4-dithiin sulfur units, as these 8 π -electron, antiaromatics offer rich reactivities. Besides various reactions on the ethene and S functions, ring contraction can occur to form the 6e⁻ aromatic thiophenes;^{26,27} the alternative, 1,3-dithiole radical^{28,29} product (Scheme 1) has not been generated from dithiin precursors, but would enrich radical-containing MOF solids.³⁰⁻⁴⁵

The tailorable spatial order of solid state frameworks offers unique opportunity to trap reactive species and to channel reaction pathways.⁴⁶⁻⁵⁴ Notably, Matsuda and Ma reported spatially isolated carbene

sites at the midpoints of the long linkers in a rigid open MOF scaffold,⁵⁵ and their higher decomposing temperature (170 K), relative to the control carbene species (80 K; in a frozen matrix of 2-methyltetrahydrofuran). Also, similarly anchored -SI and -SH groups on porous MOF grids had been explored to prevent, respectively, disproportionation (into -SS- and I₂),⁵⁶ and poisoning the Pd centers of the leach-free heterogeneous MOF catalyst.⁵⁷ In these very open nets, the far-apart, isolated linkers experience lesser steric interaction from one another, and the reactivity control by molecular packing (*e.g.*, topochemistry) is therefore weakened.

To better exploit the solid-state reactivity of the linker molecules, the spatial confinement in the less open, almost (but not quite) close packed MOF matrix of EuTTA is worthy of note. Namely, the arranged linker molecules here are slightly spaced apart (*e.g.*, by *ca.* 1.0 Å above VDW contact) to allow some wiggle room for reactions to occur, while the spatial restriction greatly narrows down the reaction pathways to improve product selectivity.

Results

Framework formation and Crystal structure. Single crystals of EuTTA were obtained by reacting H₂TTA with EuCl₃•6H₂O in water and acetonitrile (4:1, v/v) at 150°C for 48 hours. The yellow crystals are not photoluminescent.⁵⁸ The X-ray structure of the 3D net of EuTTA features parallel Eu-carboxyl rods (along the *c* axis) in a quadrangle array (Fig. 1). The neighboring Eu atoms exhibit alternating distance (3.948 and 4.517 Å): the short pair is straddled by four carboxyl groups, and the long pair by two carboxyl groups and one aqua bridge. Together the asymmetric formula of the unit cell is Eu(C₁₂H₄O₄S₄)_{1.5}(H₂O)_{0.5}, with one centric TTA piece (with lower site multiplicity) contributing only as half. The bulk sample features the same crystalline phase (PXRD patterns in Fig. 2A). Elemental analysis found [C (31.65%), H (1.24%), S (24.62%)], fitting the formula Eu₂(C₁₂H₄O₄S₄)₃(H₂O)₂ with a calculated profile: C (31.77%), H (1.18%), S (28.26%).

The spacing of the TTA molecules along the Eu-carboxyl rod is also uneven (Fig. 1C): with a close pair (interplanar gap: 3.7 Å; the pair is related by a center of symmetry, but each being non-centric) alternating with the (centric) TTA at *ca.* 4.6 Å. The C₂H₂ flank of the latter is disordered over two sets of positions, in line with the more open setting. The opening, however, is limited: it allows the atoms to wiggle more, but not N₂ or CO₂ guests to sorb (Figure S18).

The impact on reactivity, notably, is decisive. For when the EuTTA crystal is heated to 230 °C (to form EuTTA-230), the loose (centric) TTA loses one (S or C) atom on each wing, and forms benzodithiophene (BDT) or bis(dithiole) rings (as illustrated in Scheme 1 and Figures 1C); the other two (*i.e.*, the close pair of) TTA, by comparison, remain unchanged. As evidence, the X-ray structure is telling (Figure 1C). The heated sample (EuTTA-230) retains the same net and the same space group [C2/c: 16.385(3), 16.484(3), 16.295(3) Å, 116.11(3)°; cell volume: 3952.0 Å³], *cf.* the pristine EuTTA [16.5676(15), 16.3937(14), 16.2839(14) Å; cell volume: 4045.5 Å³]. Revealingly, the sulfur atoms on the transformed linker become

only partially occupied (*i.e.*, contrasting the full occupancy of the dithiin S sites in the other two unchanged TTA pieces). The disordering of the S and C sites on the transformed linker, however, precludes a qualitative assignment of the benzodithiophene (BDT) or bis(dithiole) components. But the presence of the reported *anti*-benzo[1,2-b:5,4-b']dithiophene molecule (*anti*-BDT)⁵⁹ is supported by solution NMR data (from the EuTTA-230 sample dissolved in HF/DMSO-*d*₆; mostly dissolved, but with a little black solid remaining), see Figure S20, while the distinct EPR signal of the EuTTA-230 solid (Figure S24) is consistent with formation of the open-shell dithiole species. Besides the *anti*-BDT signals, the NMR data (Figure S20) also feature additional peaks, suggesting other molecular products in the bulk sample, including possibly the *syn*-BDT isomer and the halfway, dithiin-benzothiophene product DTBT as drawn in Figure S20.

The ring contraction lessens the steric repulsion on the carboxyl groups, and more coplanarity is seen between the benzothiophene and carboxyl moieties, with the dihedral angle (5.16°) much smaller than that of the dithiin-based TTA precursor (48.65°). The coplanarity helps align the benzothiophene length along the Eu-carboxyl rod, and swings its wing atoms closer to the neighboring dithiin molecules (at C•••C contact of 3.49 Å). The wiggle room for the molecules is therefore compressed, apparently stopping the two remaining TTA linkers from undergoing reactions at this temperature (230°C).

At higher temperatures (*e.g.*, 350°C for 2 hours), the remaining TTA linkers also react. Specifically, the resulted crystals (EuTTA-350) become darker (black) (Figure S17) and slower to dissolve in HF/DMSO-*d*₆; and ¹H NMR (Figure S20) of the dissolved portion (mostly dissolved, with some black solid remaining—more than the EuTTA-230 case) features only two pairs of peaks (one from the known *anti*-BDT, the other possibly from the *syn*-BDT isomer), without any dithiin C₂H₂ signal from the TTA molecule remaining.

Radical analysis of EuTTA-350. Most notable of the EuTTA-350 crystals is the stronger and stable paramagnetic signals. The EPR signal centers at $g = 2.002$ (Figure 2B), and is indicative of organic radicals. No EPR peaks for Eu(II) (*e.g.* $g \approx 2.0, 2.8, 3.4, 4.5$ and 6.0)⁶⁰ were detected, with the $4f^6$ Eu³⁺ (in the ⁷F₀ ground state) being diamagnetic/EPR-silent. No reduction of Eu(III) to Eu(II) during thermal treatment was thus found, which is also confirmed by the X-ray photoelectron spectroscopy (XPS) signals at 1165.5 and 1135.4 eV corresponding to the Eu(III) 3d_{3/2} and 3d_{5/2} peaks which are also observed in the EuTTA precursor (Figure 2C, S21, S22).^{61,62} The EPR signal of EuTTA-350 remains significant after heating at 300 °C in air for 2 hours, or boiling in water for 24 hours (Figure 3A). Notably, the organic components of EuTTA-350 can be extracted into an acidic solution (*e.g.*, into DMSO/HCl), and then precipitated (*e.g.*, by adding water) to give an organic solid that retains strong EPR signal, further showcasing the stability of the radical species thereof (Figure S25).

The stronger EPR signal suggests further formation of 1,3-dithiole-based radicals in EuTTA-350, *i.e.*, from the two remaining TTA linkers, in addition to the radical species initially formed (*e.g.*, at 230°C, as in the above mentioned EuTTA-230). The strong paramagnetism complicates the direct detection of the dithiole products by NMR. To verify the formation of a bis(dithiole) molecule, it is key to demonstrate the retention

of the four sulfur atoms (*vs.* only two S atoms in the benzodithiophene case). For this, oxidative treatment to convert the bis(dithiole) into the more tractable tetrasulfonic acid derivative (Figure S26)⁶³ was attempted. Specifically, the soluble fraction of the EuTTA-350 crystals were first extracted into DMSO/HCl, and then precipitated out by adding water. The black precipitate was treated with 30% H₂O₂ to give a red-brown solution (with some red solid remaining); the solution was then evaporated, and the residue (dissolved in D₂O) was found by both ¹H and ¹³C NMR to feature the expected tetrasulfonic acid derivative (Figure S26).

Single crystal X-ray diffraction of EuTTA-350 remains strong (albeit with peaks of poor shapes), and indicates the structural integrity of the Eu-carboxylate framework. But the severe disorder on the linker portion makes it hard to pinpoint the C and S atoms on the two S-heterocycle wings (see the .res file for a plausible but non-definitive model for the flanking S/C sites). So the X-ray data of EuTTA-350 do not clarify the crosslinks among the linker molecules; but the lowered solubility of the EuTTA-350 crystals in HF/DMSO-*d*₆ (relative to the readily soluble EuTTA) suggests some degree of crosslinking might have occurred, as is tentatively proposed in Figure S27; the scheme therein features the formula Eu₄(C₂₄H₆O₈S₄)(C₂₃H₆O₈S₈)₂(H₂O)₁₄, and a calculated elemental profile [C (30.64%), H (1.69%), S (23.37%)] consistent with the elemental analysis results [C (30.71%), H (1.85%), S (25.02%)] for EuTTA-350.

Variable-temperature magnetic susceptibility measurement of EuTTA and EuTTA-350 were carried out at a dc field of 1000 Oe at 2–300 K. From M_T versus T plots (Fig. 2D), M_T of EuTTA is 2.38 cm³ K mol⁻¹ at room-temperature and decreased to 0.025 cm³ K mol⁻¹ at 2 K. The paramagnetism of EuTTA in 2–300 K is caused by coupling between nonmagnetic ⁷F₀ ground state and closely lying ⁷F₁ excited state of Eu(III),⁶⁴ so the M_T contributed by Eu(III) is 2.36 cm³ K mol⁻¹. As for EuTTA-350 [molar mass 1209: 90% of that of EuTTA, Eu₂(C₁₂H₄O₄S₄)₃(H₂O), 1343; based on TGA weight loss of 10% from EuTTA to EuTTA-350, Figure S14], the M_T is 10.06 cm³ K mol⁻¹ at room-temperature and decreased to 8.09 cm³ K mol⁻¹. The decrease is caused by Eu(III), while the remaining M_T value of 8.09 cm³ K mol⁻¹ can be ascribed to the organic radicals in EuTTA-350. The corresponding effective magnetic moment $\mu_{\text{eff}} = (8M_T)^{1/2} = 8.04$ B.M., which approximates that of 6 unpaired electrons: $\mu_{\text{eff}} = g\sqrt{S(S+1)} = 6.93$ (S = 6/2 = 3, with g = 2). Because of little linker loss (*e.g.*, < 5% from TGA data, Figure S14) from EuTTA to EuTTA-350, we assume the formula unit of EuTTA-350 to retain 3 linkers; the above numbers thus suggest each linker bearing 2 unpaired electrons as a diradical. The biradical is fitting for the bis(dithiole) product and was also consistent with the tetrasulfonic derivative (Figure S26); As for the benzodithiophene (BDT) components, radicals can arise and stabilize from thiophene crosslinks as illustrated in Figure S27.⁶

DFT calculation. For illustration theoretical calculation was conducted on the protonated form of the bis(dithiole) diradical (Figure 2E). The results show that spin densities locate mainly on the two sulfur-flanked C atoms (0.71 and 0.63 spin, respectively, Table S1); the S atoms also take up almost the remaining spin densities (0.28 and 0.17 spin on each set of S atoms, Table S1). Atoms of the benzenoid

core also share spin densities but these are far smaller than the spin densities on the side S–C–S moieties. The spin natural orbitals (SNOs) of two independent spins (Figure 2E) suggest that (1) two spins mainly localize on the S–C–S wings (71.72% and 88.48% orbital contribution, Table S2) and (2) the two spins are unlike to mix as reflected by the separate orbitals occupied by each spin. The spin densities and SNO results thus consistently indicate the diradicals to mostly localize on the S–C–S units of the dithiole rings.

Photothermal conversion and water evaporation. The radical-rich EuTTA-350 solid strongly absorbs across the broad visible/near-infrared regions (see Fig. 3B for the diffuse reflectance spectra), suggesting photothermal conversion uses. Also, the thermal conductivity of EuTTA-350 was found to be as low as $0.2 \text{ W K}^{-1} \text{ m}^{-1}$ (like that of rubber or mineral oil) at room temperature (Figure S28), indicating good thermal insulating property suited for photothermal conversion applications. As is monitored by an infrared camera, the temperature of EuTTA-350 powder rises rapidly under a xenon lamp (1 kW m^{-2} , 420–2500 nm; to simulate 1-sun illumination): as shown in Figs. 4A and 4B, within 480 seconds, it increases by 47°C to reach 69.2°C , which is a highest jump among MOF materials, second only to the Zr-Fc solid (Figure S30).^{65–68} By comparison, EuTTA and EuTTA-230 reach only 41.4°C and 47.6°C , respectively, under the same conditions. In addition, the photothermal performance of EuTTA-350 is stable: in all 5 illumination cycles tested, the temperature consistently rises to 65°C within in 480 seconds (Fig. 4C); and PXRD indicates the sample remains crystalline afterwards (Figure S29).

So we use EuTTA-350 to build a solar-driven water evaporation device (Figure S35). As EuTTA-350 is light-weight and hydrophobic (with a high contact angle of 85.4° ; Figure S36), its powder disperses to form a floating thin film, facilitate heat transfer to the water body for efficient interfacial evaporation. Under 1-sun (1 kW m^{-2}) exposure in air (using 50 mg of EuTTA-350), the evaporation rate (see the plot in Fig. 4D, see also plots in Figure S33 and S34 for other amounts of EuTTA-350) can reach $1.44 \text{ kg m}^{-2} \text{ h}^{-1}$, 4 times that of pure water ($0.36 \text{ kg m}^{-2} \text{ h}^{-1}$), and also better than EuTTA ($0.62 \text{ kg m}^{-2} \text{ h}^{-1}$) and EuTTA-230 ($1.12 \text{ kg m}^{-2} \text{ h}^{-1}$), with the temperature equilibrating at 47.4°C after 1 hour (Figure S31). The infrared thermal image showed that the energy conversion takes place at the MOF layer (Figure S31). The solar-driven water evaporation efficiency is calculated to be 97.9%,⁶⁹ among the highest of all photothermal materials (Fig. 4E, Table S3).^{67,68,70–78}

Conclusion

In summary, the thermally induced ring contraction of the dithiin units to form thiophene and dithiole functions in the MOF solid of EuTTA is clearly supported by both X-ray and NMR data (*e.g.*, with the dithiole products in EuTTA-350 being evidenced by its tetrasulfonic derivative; Figure S26). The bonding/connection between the dithiole/thiophene units across the linker molecules, however, proves harder to characterize, because of the severe disorder in the crystal structures, and because of the likely reaction among the radical species once dissolved into solutions. Nevertheless, the extraordinary persistence of the resulted radical species is impressive, which, in a practical note, also imparts strong

visible/near IR absorption and enables efficient photothermal conversion for solar steam generation applications. On a broader front, advances can be envisioned from dithiin-equipped linker molecules (as exemplified here by TTA), as these offer a unique blend of stability (in air and water as protected S functions) and reactivity (from the ethene and the flanking S units) for material design. Building on this important lead, one can integrate the dithiin function into many other framework systems, in order to better synergize the amazing interplay of porosity, open-shell/radical features and crosslinks, and to open new vistas for electronic and magnetic properties in the solid state.

Methods

Crystallization and activation of EuTTA. H₂TTA (6.0 mg, 0.0173 mmol) and EuCl₃·6H₂O (8.4 mg, 0.023 mol) was loaded into a glass tube. Then a water/acetonitrile (4:1, 1 mL) mixed solution was added and the tube was sealed with an oxyhydrogen flame. The glass tube was placed in an oven at 150°C for 48 hours, during which yellow crystals slowly formed. After the sealed tube was heated for 48 hours, it was cooled to room temperature over 4 hours. The yellow crystals were collected and washed with acetonitrile several times and air-dried to obtain yellow EuTTA crystals. For elemental analysis, the crystals were activated *via* Soxhlet extraction with methanol for two days, and then placed in vacuum at 80°C for 10 hours. [C (31.65%), H (1.24%), S (24.62%), N (0.29%)]; a fitting formula can be determined to be Eu₂(C₁₂H₄O₄S₄)₃(H₂O)₂, which gives a calculated profile of [C (31.77%), H (1.18%), S (28.26%)]. The synthesis of the new organic linker H₂TTA can be found in Supplementary Fig. S1 and Supplementary Methods.

Synthesis of EuTTA-230 crystals. 100 mg EuTTA as-made crystals were washed with acetonitrile (3 × 2 mL) and soaked in acetonitrile (3 × 3 mL, replaced by fresh acetonitrile after 12 hours each time). The resulting crystals were filtered and then evacuated at 70°C for 8 hours. Then the crystal sample was heated in a tube furnace under a nitrogen atmosphere at 230°C for 10 hours. Heating rate: 5°C/minute.

Synthesis of EuTTA-350 crystals. The previous steps are the same as above. Then the crystal sample was heated in tube furnace at nitrogen atmosphere at 350°C for 2 hours. Heating rate: 5°C/minute.

Photothermal conversion measurement. EuTTA-350 powder (70 mg) was spread on a quartz slide to form a thin circular film (thickness *ca.* 2 mm) with the largest possible surface area (diameter of 1.6 cm), which was set up at a distance of 30 cm from the xenon lamp (AM 1.5 G, PLS-SXE300+), corresponding to an irradiance of 1 kW m⁻² (1-Sun). An infrared camera was used to take the infrared photographs of the EuTTA-350 MOF powder, *e.g.*, when the illumination was turned on and off.

Solar-Driven Vapor Generation Experiments. The EuTTA-350 powder was floated on water in a quartz beaker (see Figure S31 below). Sunlight was simulated by a xenon lamp (PLS-SXE300+) with an optical filter (AM 1.5 G) and used to irradiate the sample under specific power density. The mass change of the water was recorded by an electronic balance (accuracy of 0.00001 g). An IR camera was used to measure

the temperature. All experiments were conducted at ambient temperature of 22°C and the humidity of 65%.

Declarations

Acknowledgements

This work was supported by Local Innovative and Research Teams Project of Guangdong Pearl River Talents Program (2017BT01Z032), the National Natural Science Foundation of China (21871061), the Foundation of Basic and Applied Basic Research of Guangdong Province (2020B1515120024), Science and Technology Planning Project of Guangdong Province (2021A0505030066), and Science and Technology Program of Guangzhou (201807010026). Z.X. acknowledges a GRF grant from the Research Grants Council of HKSAR (CityU 11303519). We also thank Dr. Matthias Zeller and Dr. Wei-Ming Liao for their valuable help with this work.

Author contributions

X.Y., L.C., K.L., Z.X. and J.H. conceived and designed the experiments. X.Y. and Y.W. synthesized the materials. D.C. and Z.X. Analysed the crystal structure. L.C. and S.Z. Analysed the EPR and magnetic data. X.Y., L.C., Z.F., Y.H., K.L., Z.X. and J.H. analysed the data and co-wrote the manuscript. All authors discussed the results and commented on the manuscript.

Additional information

Accession codes: The X-ray crystallographic coordinates for structure reported in this study has been deposited at the Cambridge Crystallographic Data Centre (CCDC), under deposition number 2132960 and 2132961. These data can be obtained free of charge from the Cambridge Crystallographic Data Centre via www.ccdc.cam.ac.uk/data_request/cif.

Supplementary Information accompanies this paper at <http://www.nature.com/naturecommunications>

Competing financial interests: The authors declare no competing financial interests.

Reprints and permission information is available online

at <http://npg.nature.com/reprintsandpermissions/>

References

1. Chen, Z. X., Li, Y. & Huang, F. Persistent and Stable Organic Radicals: Design, Synthesis, and Applications. *Chem* **7**, 288–332 (2021).
2. Hicks, R. G. What's new in stable radical chemistry? *Org. Biomol. Chem.* **5**, 1321–1338 (2007).
3. Zhang, K., Monteiro, M. J. & Jia, Z. Stable organic radical polymers: synthesis and applications. *Polym. Chem.* **7**, 5589–5614 (2016).

4. Nguyen, T. P. *et al.* Polypeptide organic radical batteries. *Nature* **593**, 61–66 (2021).
5. Xie, Y., Zhang, K., Yamauchi, Y., Oyaizu, K. & Jia, Z. Nitroxide radical polymers for emerging plastic energy storage and organic electronics: fundamentals, materials, and applications. *Mater. Horiz.* **8**, 803–829 (2021).
6. Kawata, S. *et al.* Singlet Fission of Non-polycyclic Aromatic Molecules in Organic Photovoltaics. *Adv. Mater.* **28**, 1585–1590 (2016).
7. Zeng, M. *et al.* Dopamine semiquinone radical doped PEDOT:PSS has enhanced conductivity, work function and performance in organic solar cells. *Adv. Energy Mater.* **10**, 2000743 (2020).
8. Phan, H. *et al.* Room-Temperature Magnets Based on 1,3,5-Triazine-Linked Porous Organic Radical Frameworks. *Chem* **5**, 1223–1234, (2019).
9. London, A. E. *et al.* A high-spin ground-state donor-acceptor conjugated polymer. *Sci. Adv.* **5**, eaav2336 (2019).
10. Thorarinsdottir, A. E. & Harris, T. D. Metal-Organic Framework Magnets. *Chem. Rev.* **120**, 8716–8789 (2020).
11. Minguez Espallargas, G. & Coronado, E. Magnetic functionalities in MOFs: from the framework to the pore. *Chem. Soc. Rev.* **47**, 533–557 (2018).
12. Lu, B. *et al.* Stable radical anions generated from a porous perylenediimide metal-organic framework for boosting near-infrared photothermal conversion. *Nat. Commun.* **10**, 767 (2019).
13. Chan, J. M. W. *et al.* Self-Assembled, Biodegradable Magnetic Resonance Imaging Agents: Organic Radical-Functionalized Diblock Copolymers. *ACS Macro Lett.* **6**, 176–180 (2017).
14. Kim, Y. *et al.* Highly Stable 1,2-Dicarbonyl Radical Cations Derived from N-Heterocyclic Carbenes. *J. Am. Chem. Soc.* **143**, 8527–8532 (2021).
15. Ji, L., Shi, J., Wei, J., Yu, T. & Huang, W. Air-Stable Organic Radicals: New-Generation Materials for Flexible Electronics. *Adv. Mater.* **32**, 1908015 (2020).
16. Zeng, W. & Wu, J. Open-Shell Graphene Fragments. *Chem* **7**, 358–386 (2021).
17. Xiang, Q. *et al.* Stable Olympicenyl Radicals and Their π -Dimers. *J. Am. Chem. Soc.* **142**, 11022–11031 (2020).
18. Li, G. *et al.* Dearomatization Approach Toward Superbenzoquinone-Based Diradicaloid, Tetraradicaloid, and Hexaradicaloid. *Angew. Chem., Int. Ed.* **58**, 14319–14326 (2019).
19. Rana, A. *et al.* Stable Expanded Porphycene-Based Diradicaloid and Tetraradicaloid. *Angew. Chem., Int. Ed.* **57**, 12534–12537 (2018).
20. Li, Y., Jia, Z., Xiao, S., Liu, H. & Li, Y. A method for controlling the synthesis of stable twisted two-dimensional conjugated molecules. *Nat. Commun.* **7**, 11637pp, (2016).
21. Shimizu, D. & Osuka, A. Porphyrinoids as a platform of stable radicals. *Chem. Sci.* **9**, 1408–1423 (2018).
22. Chui, S. S. Y., Lo, S. M. F., Charmant, J. P. H., Orpen, A. G. & Williams, I. D. A chemically functionalizable nanoporous material $[\text{Cu}_3(\text{TMA})_2(\text{H}_2\text{O})_3]_n$. *Science* **283**, 1148–1150 (1999).

23. Li, H., Eddaoudi, M., O'Keeffe, M. & Yaghi, O. M. Design and synthesis of an exceptionally stable and highly porous metal-organic framework. *Nature* **402**, 276–279 (1999).
24. Férey, G. *et al.* A Chromium Terephthalate-Based Solid with Unusually Large Pore Volumes and Surface Area. *Science* **309**, 2040–2042 (2005).
25. Cavka, J. H. *et al.* A new zirconium inorganic building brick forming metal organic frameworks with exceptional stability. *J. Am. Chem. Soc.* **130**, 13850–13851 (2008).
26. Eisch, J. J. & Im, K. R. Hydrodesulfurization and ring contraction of sulfur heterocycles by nickel(0) complexes. *J. Organomet. Chem.* **139**, C51-C55 (1977).
27. Hu, Y. *et al.* Core-Expanded Naphthalene Diimides Fused with Sulfur Heterocycles and End-Capped with Electron-Withdrawing Groups for Air-Stable Solution-Processed n-Channel Organic Thin Film Transistors. *Chem. Mater.* **23**, 1204–1215 (2011).
28. Saha, A. *et al.* Sulfur rich electron donors - formation of singlet versus triplet radical ion pair states featuring different lifetimes in the same conjugate. *Chem. Sci.* **8**, 1360–1368 (2017).
29. Krebs, F. C., Larsen, J., Boubekur, K. & Fourmigue, M. Synthesis, properties and radical cation salts of non-centrosymmetrical tetrathiafulvalenes derived from 1,3,5,7-tetrathia-s-indacene. *Acta Chem. Scand.* **47**, 910–915, 47–0910 (1993).
30. Faust, T. B. & D'Alessandro, D. M. Radicals in metal-organic frameworks. *RSC Adv.* **4**, 17498–17512 (2014).
31. Li, Z., Liu, Y., Kang, X. & Cui, Y. Chiral Metal-Organic Framework Decorated with TEMPO Radicals for Sequential Oxidation/Asymmetric Cyanation Catalysis. *Inorg. Chem.* **57**, 9786–9789 (2018).
32. Liu, H. *et al.* Emergence of a Radical-Stabilizing Metal-Organic Framework as a Radiophotoluminescence Dosimeter. *Angew. Chem., Int. Ed.* **59**, 15209–15214 (2020).
33. Su, J. *et al.* Persistent radical tetrathiafulvalene-based 2D metal-organic frameworks and their application in efficient photothermal conversion. *Angew. Chem., Int. Ed.* **60**, 4789–4795 (2021).
34. Kimura, S. *et al.* An Open-shell, Luminescent, Two-Dimensional Coordination Polymer with a Honeycomb Lattice and Triangular Organic Radical. *J. Am. Chem. Soc.* **143**, 4329–4338 (2021).
35. van Koeveden, M. P. *et al.* Tuning Charge-State Localization in a Semiconductive Iron(III)-Chloranilate Framework Magnet Using a Redox-Active Cation. *Chem. Mater.* **32**, 7551–7563 (2020).
36. Souto, M., Strutynski, K., Melle-Franco, M. & Rocha, J. Electroactive Organic Building Blocks for the Chemical Design of Functional Porous Frameworks (MOFs and COFs) in Electronics. *Chem. - Eur. J.* **26**, 10912–10935 (2020).
37. Jellen, M. J., Ayodele, M. J., Cantu, A., Forbes, M. D. E. & Garcia-Garibay, M. A. 2D Arrays of Organic Qubit Candidates Embedded into a Pillared-Paddlewheel Metal-Organic Framework. *J. Am. Chem. Soc.* **142**, 18513–18521 (2020).
38. Collins, K. A. *et al.* Synthetic investigation of competing magnetic interactions in 2D metal-chloranilate radical frameworks. *Chem. Sci.* **11**, 5922–5928 (2020).

39. Tang, S. *et al.* Tunable Reduction of 2,4,6-Tri(4-pyridyl)-1,3,5-Triazine: From Radical Anion to Diradical Dianion to Radical Metal-Organic Framework. *Angew. Chem., Int. Ed.* **58**, 18224–18229 (2019).
40. Stephaniuk, N. T., Haskings, E. M., Arauzo, A., Campo, J. & Rawson, J. M. Inclusion and reactivity of main group radicals in the porous framework MIL-53(Al). *Dalton Trans.* **48**, 16312–16321 (2019).
41. Zwolinski, K. M. & Chmielewski, M. J. TEMPO-Appended Metal-Organic Frameworks as Highly Active, Selective, and Reusable Catalysts for Mild Aerobic Oxidation of Alcohols. *ACS Appl. Mater. Interfaces* **9**, 33956–33967 (2017).
42. Murase, R. *et al.* Mixed Valency in a 3D Semiconducting Iron-Fluoranilate Coordination Polymer. *Inorg. Chem.* **56** (2017).
43. Kaim, W. & Paretzki, A. Interacting metal and ligand based open shell systems: Challenges for experiment and theory. *Coord. Chem. Rev.* **344**, 345–354 (2017).
44. DeGayner, J. A., Jeon, I.-R., Sun, L., Dinca, M. & Harris, T. D. 2D Conductive Iron-Quinoid Magnets Ordering up to $T_c = 105$ K via Heterogenous Redox Chemistry. *J. Am. Chem. Soc.* **139**, 4175–4184 (2017).
45. Xu, F. *et al.* Radical Covalent Organic Frameworks: A General Strategy to Immobilize Open-Accessible Polyradicals for High-Performance Capacitive Energy Storage. *Angew. Chem., Int. Ed.* **54**, 6814–6818 (2015).
46. Kusaka, S. *et al.* Dynamic Topochemical Reaction Tuned by Guest Molecules in the Nanospace of a Metal-Organic Framework. *J. Am. Chem. Soc.* **141**, 15742–15746 (2019).
47. Kusaka, S., Matsuda, R. & Kitagawa, S. Generation of thiyl radicals in a zinc(II) porous coordination polymer by light-induced post-synthetic deprotection. *Chem. Commun.* **54**, 4782–4785 (2018).
48. Wang, Y. *et al.* Tuning the configuration of the flexible metal-alkene-framework affords pure cycloisomers in solid state photodimerization. *Chem. Commun.* **57**, 1129–1132 (2021).
49. Hazra, A. & Maji, T. K. Guest-Responsive Reversal in Structural Transformation after a [2 + 2] Topochemical Reaction in a 3D Pillared Layer MOF: Uncovering the Role of C-H \cdots O Interaction. *Inorg. Chem.* **59**, 12793–12801 (2020).
50. Hu, F.-L. *et al.* Stereoselective Solid-State Synthesis of Substituted Cyclobutanes Assisted by Pseudorotaxane-like MOFs. *Angew. Chem., Int. Ed.* **57**, 12696–12701 (2018).
51. Zheng, Y. *et al.* Flexible interlocked porous frameworks allow quantitative photoisomerization in a crystalline solid. *Nat. Commun.* **8**, 1–6 (2017).
52. Mir, M. H., Koh, L. L., Tan, G. K. & Vittal, J. J. Single-Crystal to Single-Crystal Photochemical Structural Transformations of Interpenetrated 3D Coordination Polymers by [2 + 2] Cycloaddition Reactions. *Angew. Chem., Int. Ed.* **49**, 390–393 (2010).
53. Huang, S.-L., Hor, T. S. A. & Jin, G.-X. Photodriven single-crystal-to-single-crystal transformation. *Coord. Chem. Rev.* **346**, 112–122 (2017).
54. Khan, S., Dutta, B. & Mir, M. H. Impact of solid-state photochemical [2 + 2] cycloaddition on coordination polymers for diverse applications. *Dalton Trans.* **49**, 9556–9563 (2020).

55. Nakajo, T. *et al.* Triplet Carbene with Highly Enhanced Thermal Stability in the Nanospace of a Metal-Organic Framework. *J. Am. Chem. Soc.* **143**, 8129–8136 (2021).
56. Yee, K.-K., Wong, Y.-L. & Xu, Z. Bio-inspired stabilization of sulfenyl iodide RS-I in a Zr(IV)-based metal-organic framework. *Dalton Trans.* **45**, 5334–5338 (2016).
57. Gui, B. *et al.* Tackling poison and leach: catalysis by dangling thiol-palladium functions within a porous metal-organic solid. *Chem. Commun.* **51**, 6917–6920 (2015).
58. He, J. *et al.* A Boiling-Water-Stable, Tunable White-Emitting Metal-Organic Framework from Soft-Imprint Synthesis. *Chem. - Eur. J.* **22**, 1597–1601 (2016).
59. Citterio, A., Sebastiano, R., Maronati, A., Viola, F. & Farina, A. Oxidative dimerization of diethyl 3-thienylmalonate by high valent metal salts. Synthesis of benzo[1,2-b:4,5-b']dithiophene derivatives. *Tetrahedron* **52**, 13227–13242 (1996).
60. Alves, R. *et al.* Solid polymer electrolytes based on chitosan and europium triflate. *J Non Cryst Solids* **432**, 307–312 (2016).
61. Cai, Y., Li, X., Wu, K. & Yang, X. Electrochemical sensing performance of Eu-BTC and Er-BTC frameworks toward Sunset Yellow. *Anal. Chim. Acta* **1062**, 78–86 (2019).
62. Wang, L. *et al.* A Eu^{3+} - Eu^{2+} ion redox shuttle imparts operational durability to Pb-I perovskite solar cells. *Science* **363**, 265 (2019).
63. He, Y. *et al.* Dense Dithiolene Units on Metal–Organic Frameworks for Mercury Removal and Superprotonic Conduction. *ACS Appl. Mater.* **14**, 1070–1076 (2022).
64. Wan, Y., Zhang, L., Jin, L., Gao, S. & Lu, S. High-dimensional architectures from the self-assembly of lanthanide ions with benzenedicarboxylates and 1,10-phenanthroline. *Inorg. Chem.* **42**, 4985–4994 (2003).
65. Espín, J., Garzón-Tovar, L., Carné-Sánchez, A., Imaz, I. & MasPOCH, D. Photothermal Activation of Metal–Organic Frameworks Using a UV–Vis Light Source. *ACS Appl. Mater. Interfaces* **10**, 9555–9562 (2018).
66. Su, J. *et al.* Persistent Radical Tetrathiafulvalene-Based 2D Metal-Organic Frameworks and Their Application in Efficient Photothermal Conversion. *Angew. Chem. Int. Ed.* **60**, 4789–4795 (2021).
67. Ma, Q. *et al.* MOF-Based Hierarchical Structures for Solar-Thermal Clean Water Production. *Adv. Mater.* **31**, 1808249 (2019).
68. Ma, X. *et al.* A photothermal and Fenton active MOF-based membrane for high-efficiency solar water evaporation and clean water production. *J. Mater. Chem. A* **8**, 22728–22735 (2020).
69. Chen, G. *et al.* Biradical-Featured Stable Organic-Small-Molecule Photothermal Materials for Highly Efficient Solar-Driven Water Evaporation. *Adv. Mater.* **32**, 1908537 (2020).
70. Ma, S., Qarony, W., Hossain, M. I., Yip, C. T. & Tsang, Y. H. Metal-organic framework derived porous carbon of light trapping structures for efficient solar steam generation. *Sol. Energy Mater Sol. Cells* **196**, 36–42 (2019).

71. Ma, X. *et al.* Hierarchical Porous SWCNT Stringed Carbon Polyhedrons and PSS Threaded MOF Bilayer Membrane for Efficient Solar Vapor Generation. *Small* **15**, 1900354 (2019).
72. Zhao, X., Ma, X. & Peng, X. Carbon nanofiber stringed hierarchical porous carbon polyhedrons flexible thin films for solar vapor generation. *Appl. Phys. A* **125**, 537 (2019).
73. Guo, M.-X., Wu, J.-B., Zhao, H.-Y., Li, F.-H. & Min, F.-Q. Carbonized loofah and MOF-801 of synergistic effect for efficient solar steam generation. *Int. J. Energy Res.* **45**, 10599–10608 (2021).
74. Wang, H. *et al.* Biomimetic Ultra-Black Sponge Derived from Loofah and Co-MOF for Long-Term Solar-Powered Vapor Generation and Desalination. *Solar RRL* **5**, 2000817 (2021).
75. Ma, X. *et al.* Orientational seawater transportation through Cu(TCNQ) nanorod arrays for efficient solar desalination and salt production. *Desalination* **522**, 115399 (2022).
76. He, P. *et al.* Controllable synthesis of sea urchin-like carbon from metal-organic frameworks for advanced solar vapor generators. *Chem. Eng. J.* **423**, 130268 (2021).
77. Ma, X. *et al.* A robust asymmetric porous SWCNT/Gelatin thin membrane with salt-resistant for efficient solar vapor generation. *Appl. Mater. Today* **18**, 100459 (2020).
78. Fan, X. *et al.* A MXene-Based Hierarchical Design Enabling Highly Efficient and Stable Solar-Water Desalination with Good Salt Resistance. *Adv. Funct. Mater.* **30**, 2007110 (2020).

Scheme 1

Scheme 1 is available in the Supplementary Files section.

Figures

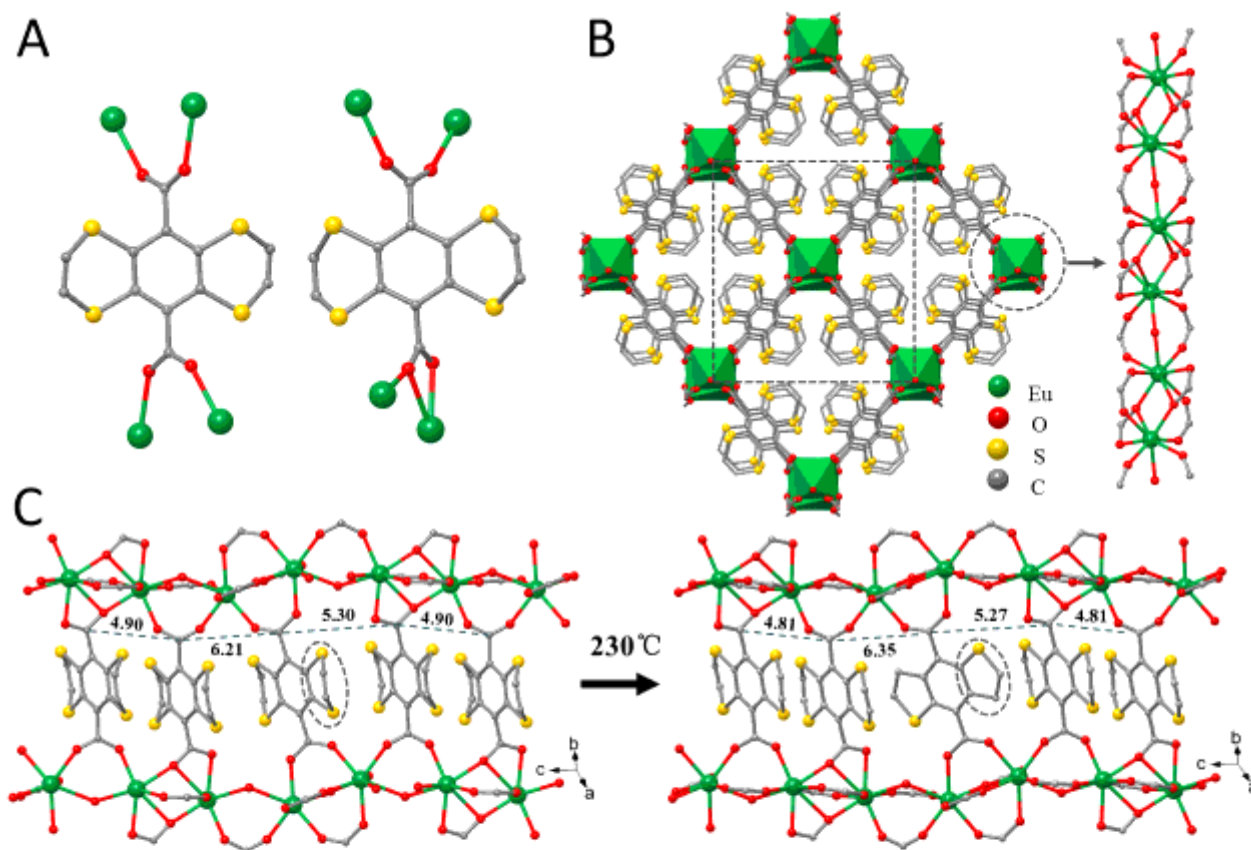


Figure 1. Single-crystal-to-single-crystal change from EuTTA to EuTTA-230: (A) Diagrammatic representation of the coordination environment of two types of coordination modes between carboxylate and Eu centers. (B) A view of EuTTA along the *c* axis, and (C) the side view of a stack of the linker molecules and the two associated Eu-carboxylate chains in EuTTA and EuTTA-230. The numbers (in Å) mark the spacing between the neighboring carboxyl C atoms. Note: the thiophene portion in panel C is disordered and can also be refined as a dithiole unit.

Figure 1

Single-crystal-to-single-crystal change from EuTTA to EuTTA-230: (A) Diagrammatic representation of the coordination environment of two types of coordination modes between carboxylate and Eu centers. (B) A view of EuTTA along the *c* axis, and (C) the side view of a stack of the linker molecules and the two associated Eu-carboxylate chains in EuTTA and EuTTA-230. The numbers (in Å) mark the spacing between the neighboring carboxyl C atoms. Note: the thiophene portion in panel C is disordered and can also be refined as a dithiole unit.

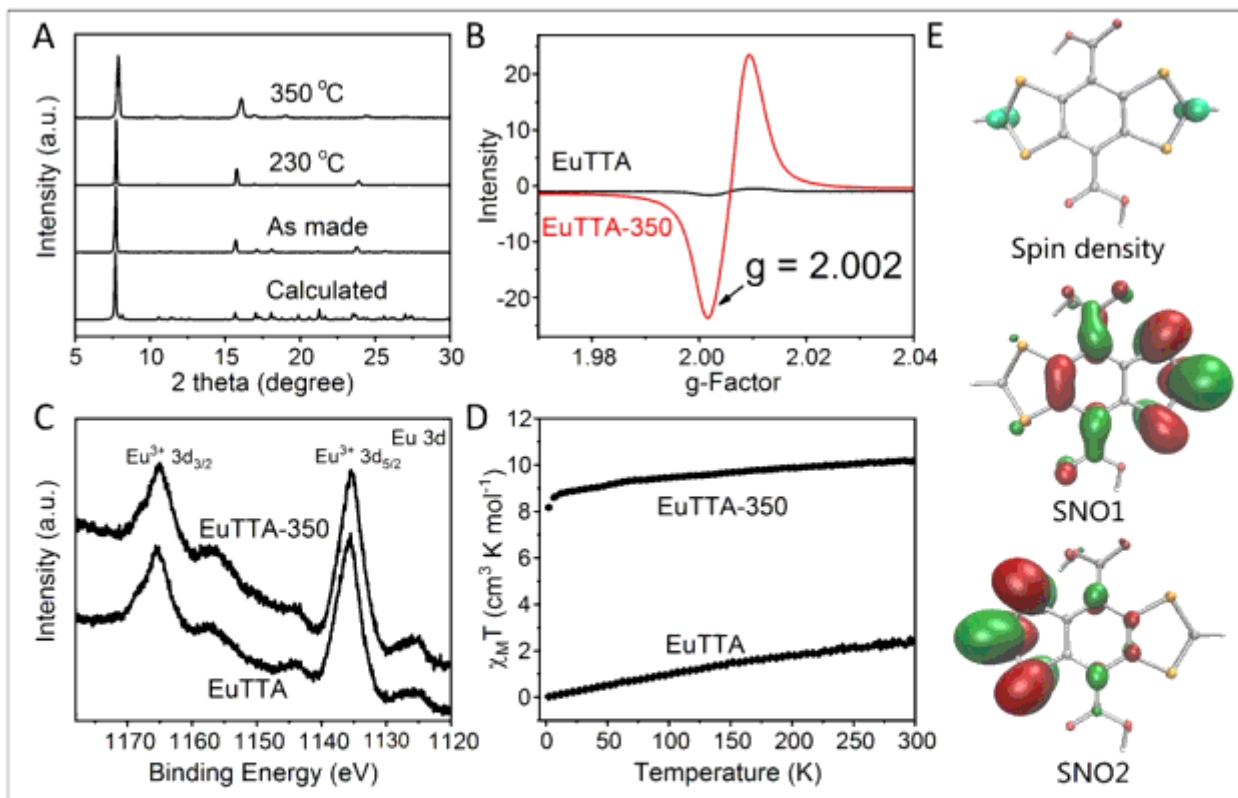


Figure 2. (A) Powder X-ray diffraction patterns of EuTTA. (B) Solid-state EPR spectra of EuTTA and EuTTA-350 at 300 K. (C) The XPS spectra of Eu 3d of EuTTA and EuTTA-350. (D) Plots of $\chi_M T$ versus T for EuTTA and EuTTA-350 at 1000 Oe field. (E) Spin densities distribution of the triplet biradical bis(dithiole) with an isosurface value of 0.02 au. and calculated SNOs of independent spins (red area stand for negative value and green area for positive value).

Figure 2

(A) Powder X-ray diffraction patterns of EuTTA. (B) Solid-state EPR spectra of EuTTA and EuTTA-350 at 300 K. (C) The XPS spectra of Eu 3d of EuTTA and EuTTA-350. (D) Plots of $\chi_M T$ versus T for EuTTA and EuTTA-350 at 1000 Oe field. (E) Spin densities distribution of the triplet biradical bis(dithiole) with an isosurface value of 0.02 au. and calculated SNOs of independent spins (red area stand for negative value and green area for positive value).

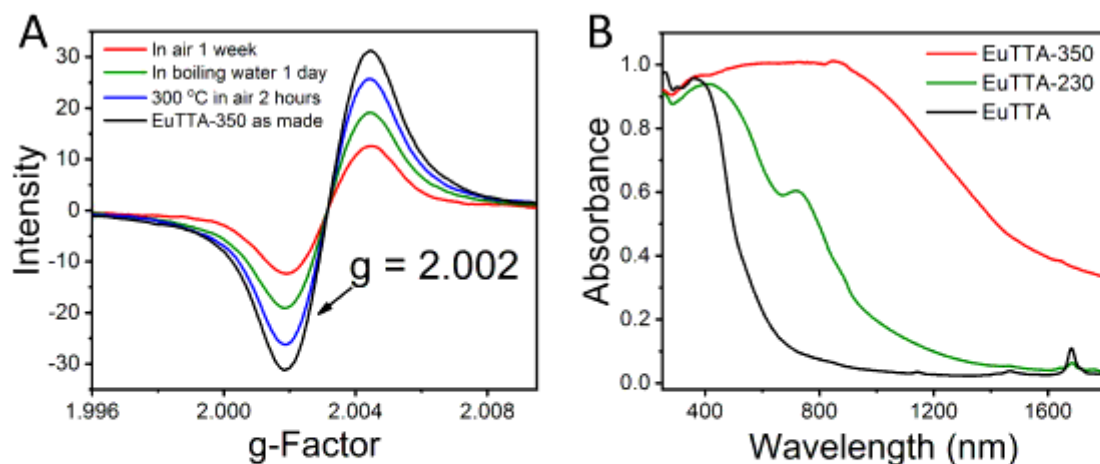


Figure 3. (A) The solid-state electron paramagnetic resonance (EPR) spectrum of EuTTA-350 treated under different conditions. (B) UV-Vis-NIR absorption of EuTTA, EuTTA-230 and EuTTA-350 powders.

Figure 3

(A) The solid-state electron paramagnetic resonance (EPR) spectrum of EuTTA-350 treated under different conditions. (B) UV-Vis-NIR absorption of EuTTA, EuTTA-230 and EuTTA-350 powders.

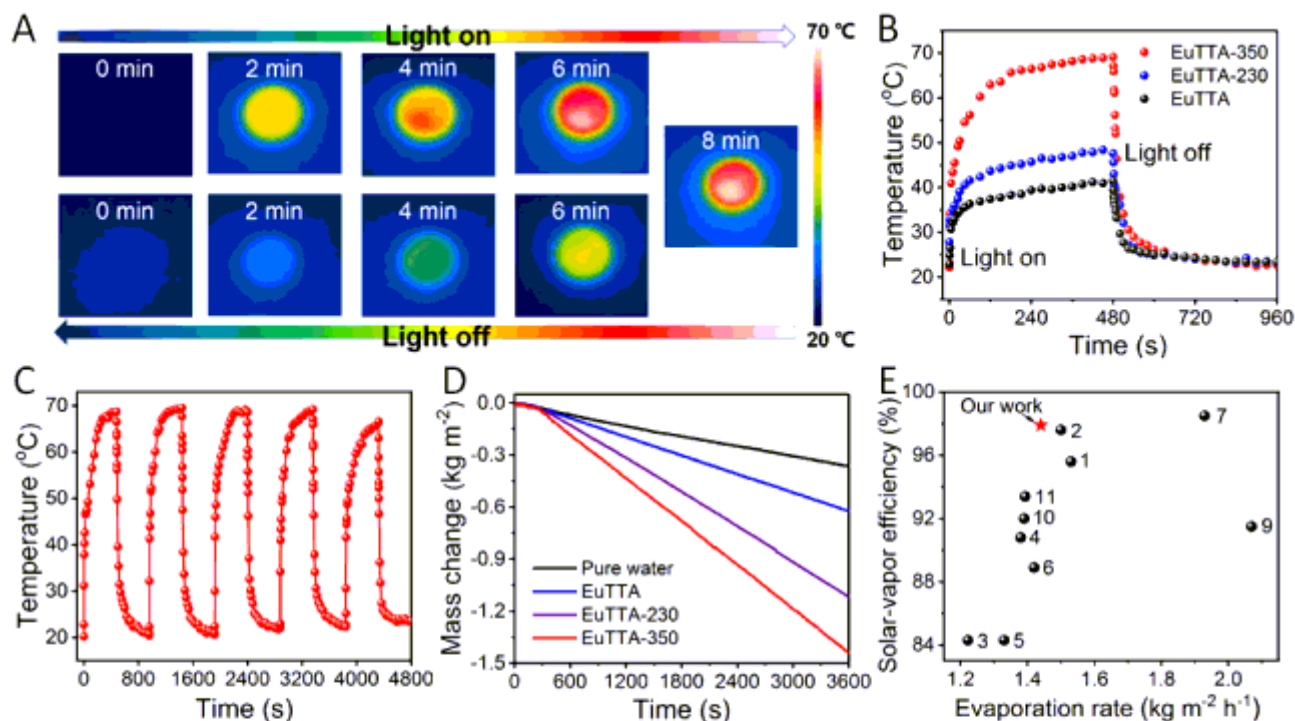


Figure 4. (A) IR thermal images of EuTTA-350 powder (50 mg) under Xenon lamp (1 kW m^{-2}) and then with Xenon lamp turned off. (B) Photothermal conversion behavior of EuTTA, EuTTA-230 and EuTTA-350 powder under 1 sun irradiation within 480 seconds. (C) Anti-photobleaching property of EuTTA-350 powder during 5 cycles of heating-cooling. (D) Water evaporation under simulated sunlight with an intensity of 1 kW m^{-2} (1 sun). (E) Comparison of the performances of MOF-based solar water evaporators reported so far.

Figure 4

(A) IR thermal images of EuTTA-350 powder (50 mg) under Xenon lamp (1 kW m^{-2}) and then with Xenon lamp turned off. (B) Photothermal conversion behavior of EuTTA, EuTTA-230 and EuTTA-350 powder under 1 sun irradiation within 480 seconds. (C) Anti-photobleaching property of EuTTA-350 powder during 5 cycles of heating-cooling. (D) Water evaporation under simulated sunlight with an intensity of 1 kW m^{-2} (1 sun). (E) Comparison of the performances of MOF-based solar water evaporators reported so far.

Supplementary Files

This is a list of supplementary files associated with this preprint. Click to download.

- [Onlinedrawingimage1.png](#)
- [EuTTASupportingInformation.pdf](#)

- [EuTTA.cif](#)
- [EuTTACheckCIF.pdf](#)
- [EuTTA230.cif](#)
- [EuTTA230CheckCIF.pdf](#)
- [crystallographyhklfileforEuTTA350asSI.txt](#)
- [crystallographyresfileforEuTTA350asSI.txt](#)